T. Bierkandt, P. Oßwald, T. Schripp, M. Köhler, Experimental investigation of soot oxidation under well-controlled conditions in a high-temperature flow reactor, Combustion Science and Technology 191 (2019) 1499-1519.

The original publication is available at www.informaworld.com

https://doi.org/10.1080/00102202.2018.1554651

Or use open URL link
http://www.informaworld.com/openurl?genre=article&issn= 1563-521X &volume=191&issue=9&spage=1499;

Experimental investigation of soot oxidation under well-controlled conditions in a high-temperature flow reactor

Thomas Bierkandt*, Patrick Oßwald, Tobias, Schripp, Markus Köhler

Institute of Combustion Technology, German Aerospace Center (DLR), Pfaffenwaldring 38-40, 70569 Stuttgart, Germany

*Corresponding author: thomas.bierkandt@dlr.de

Abstract

Oxidation by molecular oxygen of freshly-produced soot from a flat ethylene-air-flame is investigated under well-controlled conditions in a flow reactor at 773–1273 K and atmospheric pressure. Soot particles are characterized before and after oxidation by electrical mobility technique. In addition to the size-classified soot number density, the molecular gas-phase species are obtained simultaneously by molecular-beam mass spectrometry. Oxidation behavior of soot particles as well as some hydrocarbon species sampled from the soot source was determined quantitatively. Oxygenated species are formed as molecular intermediates during the oxidation process inside the reactor. Different particle size distributions have been investigated by varying the sampling position and equivalence ratio of the flame. Oxidation of soot starts at different temperatures, but is clearly separated from oxidation of flame species starting earlier at lower temperatures. Soot oxidation rates were calculated and comparison with the Nagle-Strickland-Constable model indicates that the investigated flame-sampled soot is more reactive than graphite under the investigated conditions. The presented dataset may help to validate existing soot models.

Keywords

Soot oxidation; oxidation rate; flow reactor; particle size distribution; molecular-beam mass spectrometry

Introduction

Soot is formed in combustion by coagulation and growth of polycyclic aromatic hydrocarbons (PAHs) during the incomplete combustion of hydrocarbons (Bockhorn, 1994). Besides understanding the formation of soot, the kinetics of soot oxidation is also of crucial importance. Soot oxidation is a process that reduces the soot mass by converting the soot particles to the oxidation products CO and CO_2 and takes place on the surface of the solid particles (Omidvarborna et al., 2015). Oxidation of soot occurs parallel in all stages of the soot formation process itself under typical flame conditions (Echavarria et al., 2012). Depending on the boundary conditions, both molecular oxygen (O_2) and the hydroxyl (OH) radical can play the dominant role during soot oxidation. In technical combustion devices, zones with high oxygen content and already formed soot particles can be identified, so that soot oxidation by molecular oxygen becomes relevant. For example, conventional combustors in aero engines are designed and operated to reduce the formation of NO_x (Liu et al., 2017) following the rich-quench-lean (RQL) concept. Three different zones can be identified: (1) A rich-burning zone at the inlet of the combustor, (2) the mixing zone, i.e., a region of rapid quenching by additional air, and (3) the lean-burning zone. Soot is formed in the fuel-rich, primary combustion zone at the inlet of the combustor where the oxygen content is small and the temperature moderate. Further downstream, a secondary air stream is added rapidly. The transition from fuel-rich to lean conditions is characterized by only short residence times to avoid the formation of NO_x under stoichiometric conditions. The third region is characterized by local excess of air. In this region, soot oxidation by molecular

oxygen will be important and cannot be neglected. The majority of the previously formed soot is therefore oxidized by the injection of secondary air before the burnt gas enters the turbine. The soot oxidation by molecular oxygen is strongly influenced by the temperature and the oxygen partial pressure as supposed by Nagle and Strickland-Constable (1962) for the oxidation of pyrolytic graphite. At temperatures below 2000 K, the oxidation rate shows exponential temperature dependence, i.e., Arrhenius behavior (Park and Appleton, 1973), and does not depend strongly on the partial pressure of O_2 (Fenimore and Jones, 1967), while at higher temperatures the importance of the oxidation by O_2 increases with partial pressure of oxygen. The soot oxidation rate then shows a local maximum (Park and Appleton, 1973). A deeper understanding of the soot oxidation processes is therefore crucial to predict the resulting soot fraction in the exhaust of such combustion devices. Further oxidative agents which are also associated with soot oxidation are CO_2, H_2O, NO, and the oxygen atom (Garo et al., 1990; Ghiassi et al., 2016).

The oxidation of flame soot (Camacho et al., 2015; Higgins et al., 2002; Liu et al., 2018; Jung et al., 2004; Ma et al., 2013; Nienow et al., 2005) and diesel soot (Higgins et al., 2003) by molecular oxygen was intensively investigated before for different temperature regimes and partial pressures of oxygen in flow tube reactors by mobility analysis and/or transmission electron microscopy (TEM). Further studies also focused on the oxidation of carbon black by O_2 measured in shock-tubes (Cadman and Denning, 1996; Park and Appleton, 1973; Roth et al., 1991), the oxidation of soot which was produced by pyrolysis (Vander Wal and Tomasek, 2003), and the oxidation of graphite (Nagle and Strickland-Constable, 1962; Walls and Strickland-Constable, 1964). The oxidation of soot was also studied directly in flames by optical methods (Garo et al., 1990; Kim et al., 2008; Neoh et al., 1985; Puri et al., 1994), in two-stage burner setups to isolate the soot formation process from soot oxidation in flames (Echavarria et al., 2011; Echavarria et al., 2012; Fenimore and Jones,

1967; Ghiassi et al., 2016), and by thermogravimetric analysis (Chan et al., 1987; Gilot et al., 1993; Jaramillo et al., 2014). However, high uncertainties of soot oxidation rates in actual soot models still exist (Guo et al., 2016) and rates can differ by orders of magnitude (Khosousi and Dworkin, 2015).

Nagle and Strickland-Constable (1962) studied the oxidation of carbon between 1000–2000 °C and partial pressures of oxygen between 0.1–0.6 atm. Rods of carbon, reactor graphite, and pyrolytic graphite were electrically heated while a jet of unheated oxygen or mixtures of oxygen and nitrogen released from a tube impinged on the center of the rods. The surface of the carbon rods decomposed and the derived semi-empirical formula to determine the oxidation rate is still used today in soot models and is also known as NSC model. The work of Nagle and Strickland-Constable (1962) was later extended to 2400 °C by Walls and Strickland-Constable (1964). Park and Appleton (1973) showed by shock-tube measurements that the NSC model can also predict oxidation rates for two types of carbon black for even higher temperatures from 1700–4000 K and partial pressures of oxygen of 0.05–0.13 atm. Carbon black was chosen as representative for soot formed during the combustion of hydrocarbon fuels (Park and Appleton, 1973). Oxidation rates of propane soot at lower temperatures (770–1250 K) were investigated by Chan et al. (1987). In addition to high-temperature oxidation (> 800 °C), the investigation of soot oxidation at lower temperatures is also of interest for combustion devices. For example, temperatures of 300–700 °C can be found in the exhaust gas system of diesel motors (Stanmore et al., 2001). Vander Wal and Tomasek (2003) have studied the soot oxidation by adding soot aerosols obtained from pyrolysis of acetylene, benzene, and ethanol into the post-flame gas of a premixed, burner-stabilized flame and analyzed changes in particle diameter by TEM. Camacho et al. (2015) have measured particle size distributions (PSDs) for the oxidation of nascent soot from ethylene, *n*-heptane, and toluene flames by O_2 from 1000–7800 ppm in a flow reactor for

950, 1000, and 1050 K. Oxidation rates from Vander Wal and Tomasek (2003) and Camacho et al. (2015) were higher than predicted by the NSC model. These observations are not surprisingly, because soot has different structures in comparison to graphite and there is a relationship between carbon nanostructure and oxidative reactivity (Jaramillo et al., 2015). Even the aging of soot has an influence on its nanostructure, e.g., differences in surface microstructure of nascent soot and mature soot are known (Camacho et al., 2015), and can explain different reactivity for different types of soot. Apicella et al. (2018) have shown by high resolution transmission electron microscopy (HRTEM) and energy loss spectroscopy (EELS) that nascent soot has a quite disordered and heterogeneous structure and relatively low concentrations of sp^2 hybridized carbon in comparison to young, intermediate, and mature soot presenting spherule aggregates.

In this study, the oxidation of freshly produced soot from a C_2H_4-air-flame was investigated in a flow reactor in the lower temperature regime (773–1273 K). The molecular-beam mass spectrometry (MBMS) technique allows quantification of molecular gas-phase species in reactive environments and gives an overview of the chemical gas-phase composition without any prior knowledge. The size distribution of the soot particles was simultaneously measured by a scanning mobility particle sizer at the reactor outlet. Particles were also characterized at the reactor inlet. First experiments realized with this new setup are presented herein.

Experimental setup

Soot oxidation is investigated under well-controlled conditions in a high-temperature flow reactor, which was also used for mass spectrometric studies of the chemical gas-phase kinetics of single compounds (Kathrotia et al., 2018; Oßwald et al., 2017) and technical fuels (Köhler et al., 2018). The new soot oxidation experiment consists of five key elements: (1) A

flat-flame McKenna burner as the soot source, (2) a Dekati diluter to sample flame gases and soot particles directly from the flame, (3) the high-temperature flow reactor for soot oxidation at well-controlled conditions, (4) a particle sizer to measure the particle size distribution (PSD) before (reactor inlet) and after (reactor outlet) passing a distinct temperature profile in the reactor, and (5) a molecular-beam mass spectrometer to quantify both small molecular species originated from the sampled flame and oxidation products. The components (except the mass spectrometer) are operated at or close to ambient pressure. A schematic sketch of the experimental setup is given in Figure 1 and each component is described in more detail in the following.

Laminar, premixed ethylene-air-flames at atmospheric pressure with equivalence ratios of Φ=1.85 and 2.00 and total gas flow rates of 10 slm are used as the soot source. Flames are stabilized on a standard McKenna burner with a water-cooled, porous bronze plug (6 cm in diameter). For stabilization, a stainless steel plate is placed 30 mm above the burner surface and the whole burner setup is also in a hood. Additionally, a co-flow of air shields the flame from the surrounded air. Gas flows are precisely metered by Coriolis (C_2H_4) and thermal mass flow controllers (compressed air). Table 1 shows the detailed flame conditions. Gas flows are given in standard liter per minute (slm) at 273.15 K and 1 atm. If gases are metered by Coriolis mass flow controllers, adjusted gas flows are also given in g/min. Cold-flow velocity v is calculated at 298 K and 1 atm.

Flame gases and soot particles are sampled by a standard Dekati diluter based on ejection dilution, i.e., a high stream of nitrogen flows around the ejector nozzle behind the sampling tube. This causes a pressure drop and gases at the tip of the sampling nozzle are sucked in and are directly diluted with the nitrogen. The nitrogen mass flow at the diluter is regulated by a Coriolis flow controller and set to 20 slm (25 g/min) resulting in 1.4 bar absolute pressure at the ejection inlet. Note that this is outside the typical operation

conditions of the diluter as specified by the manufacturer and dilution ratio consequently deviate significant from the nominal value. The nozzle of the diluter is made from stainless steel with an opening diameter of 4.5 mm and is introduced into the center of the flame at two different positions to obtain different soot particle sizes. The lower position at a distance of 5 mm from the burner surface to the center of the Dekati nozzle provides a smaller inlet PSD than the higher sampling position (i.e., 25 mm above the burner). A flow rate of 0.39 slm of sampled flame gases was determined by the mass spectrometer in a calibration measurement with argon flowing through the burner matrix and a nitrogen flow of 20 slm behind the ejector nozzle of the Dekati diluter. This value gives a dilution factor of 52 under the investigated conditions. The high dilution quenches the flame reactions and minimizes diffusion loss effects of sampled particles. For the soot oxidation process, O_2 is added together with N_2 behind the ejector nozzle of the Dekati. Nitrogen is preheated to 453 K and the diluter is also heated to 393 K to prevent condensation. Gas flow of O_2 is metered by a Coriolis mass flow controller. A flow rate of 0.13 slm (0.180 g/min) O_2 (6150 ppm) is used to obtain complete oxidation of soot particles and hydrocarbons at high reactor temperatures when operating the soot source at an equivalence ratio of 1.85. For the flame with an equivalence ratio of 2.00, total oxidation of the soot particles at maximum oven temperatures (1350 K with the quartz tube reactor) was not achieved with 0.180 g/min O_2. Therefore, a higher flow rate of 0.15 slm (0.220 g/min) O_2 (7500 ppm) was needed for total oxidation in this case.

The sampled and diluted aerosol is then transferred to the reactor. Therefore, the outlet of the diluter is connected by a flexible stainless steel line (950 mm in length, 16 mm in diameter) to the reactor inlet. The inlet of the reactor is heated to 353 K. Depending on the aerosol temperature, the transfer time is no longer than 0.5 s and gases are premixed before entering the reactor. A 4-way cross is mounted at the reactor inlet. This allows continuous

monitoring of stable flame gases by connecting a quadrupole mass spectrometer (QMS, Hiden Analytical) and measurement of the PSD at the beginning and the end of the temperature ramping by the scanning mobility particle sizer (SMPS). At the outlet of the reactor, the molecular gas-phase composition is measured continuously by MBMS and the PSD by SMPS. The temperature inside the reactor is varied between 773–1273 K applying a continuous temperature ramp. Soot experiments starts at the high temperature where total oxidation is achieved under the investigated conditions and temperature then decreases with a cooling rate of -200 K/h. Temperature decay was found to provide more stable and reproducible results in comparison to ramping with increasing temperature (Oßwald and Köhler, 2015). Details about the high-temperature flow reactor, the MBMS system, and general characterization were presented by Oßwald and Köhler (2015). Briefly, the oven of the reactor has a total heated length of 1000 mm. To prevent emerging of particles at higher temperatures originating from the ceramic tube, it was replaced by a quartz tube. This limits the maximum temperature to 1350 K. Total length of the used quartz tube is 1500 mm with an inner diameter of 42 mm. The residence time of the particles inside the heated length is approx. 0.9–1.5 s depending on the temperature of the oven. Gases are sampled at the outlet of the reactor by a quartz nozzle with an opening diameter of 50 µm to determine the molecular gas-phase composition. Due to the large pressure difference during the expansion from atmosphere to 10^{-3}–10^{-4} mbar in the intermediate chamber, a molecular beam is formed. At these pressure ratios, collisions between the gas molecules quickly cease and the composition of the gas sample is preserved. The central core of the molecular beam is cut out through a skimmer and the gas sample is further expanded to about 10^{-6} mbar inside the ionization chamber of the spectrometer. Sampled molecules are ionized by electron impact ionization with an actual peak value of electron energy distribution of 11.4 eV and mass-separated by the reflectron time-of-flight (TOF) mass spectrometer (Kaesdorf) with a mass

resolution of 3000. Number of sweeps for each measuring point were $1.575 \cdot 10^6$ by 35 kHz during continuous temperature ramping. This corresponds to a temperature interval of 2.5 K per measurement.

The used scanning mobility particle sizer (SMPS) consists of an electrostatic classifier (TSI, Model 3082) and an ultrafine condensation particle counter (CPC, TSI, Model 3776). The CPC detects particles in the size range between 2.5 nm (D50) and 3 µm using butanol as condensation liquid. The electrostatic classifier consists of three parts: (1) The impactor at the inlet of the SMPS has an orifice with a diameter of 0.071 cm and provides a cutoff diameter of 610 nm for the given conditions. The adjusted inlet flow is 1.5 L/min. (2) An x-ray source (TSI, Model 3088) is used as neutralizer to make sure that all particles have a uniform and known bipolar charge distribution. (3) The differential mobility analyzer (DMA, TSI, Model 3085 or 3081) classifies the positively-charged particles in an electric field depending on their electrical mobility. By applying different voltages, certain particle size classes will pass the DMA and all particles are considered as monodisperse in size. PSDs of 2.5–150 nm (Nano-DMA 3085) and 10–1000 nm (Long DMA 3081) can be classified depending on the sheath gas flow rate in the DMA. The Nano-DMA was used for the particles sampled from the flame with Φ=1.85: At 5 mm with a sheath gas flow rate of 15 L/min (2.5–66.1 nm) and at 25 mm with a sheath gas flow rate of 7 L/min (3–101.8 nm). The Long DMA was used for the flame with Φ=2.00 with a sheath gas flow rate of 15 L/min (6.15–224.7 nm). SMPS scan time was 120 s for all measurements. Particles are sampled by a stainless steel tube which is positioned close to the tip of the quartz nozzle and is connected to the SMPS inlet by a conductive flexible tube.

Results and discussion

Temperature profiles

Temperature profiles inside the reactor were measured for two oven temperatures of 773 and 973 K with a nitrogen flow of 20 slm (25 g/min) by a K-type (NiCr-Ni) thermocouple, which is mounted inside a ceramic rod. A further calibration measurement in the isothermal zone of the reactor at x=102 cm was performed during temperature ramping from 1173–773 K. This measurement allows for deduction of a scaling law to obtain individual centerline gas-phase temperature profiles for each oven temperature passed while ramping (see Figure 2). The isothermal zone is slightly shorter than in previous measurements of Oßwald and Köhler (2015) due to the higher inlet flow (20 slm of nitrogen instead of 10 slm of argon). The procedure described by Oßwald and Köhler (2015) compensates thermal inertia and systematic deviations of the oven temperature reading. The resulting profiles can be directly used as input for a zero-dimensional flow reactor simulation (Kathrotia et al., 2018) and respective results may be compared to the experimental value at the respective temperature. Temperature profiles are provided in the supplemental material.

Characterization of particles without any oxidation process

As mentioned in the experimental section, particles from ethylene-air-flames with different equivalence ratios (Φ=1.85 and 2.00) and from different flame positions (5 and 25 mm) were sampled to obtain three different inlet particle size distributions. Sampling from 5 mm at Φ=1.85 gives a narrow particle size distribution with a count median diameter (CMD) of 12 nm (“small”) and a geometric standard deviation σ of 1.5. Sampling from 25 mm at this equivalence ratio results in a higher CMD of approx. 30 nm (“medium”) while increasing the equivalence ratio to Φ=2.00 at the same sampling height results in a CMD of 63 nm (“large”). Table 2 summarizes sampling positions, count median diameters and geometric

standard deviations for the three investigated PSDs. Because it is not the goal of the experiment to characterize the flame itself, but rather its use as particle generator, we will speak in the following of small, medium, and large PSD for particles sampled from different flame conditions and positions. In terms of flame characterization, we refer to the work of Stirn et al. (2009), who measured particle size distributions by three methods (laser-induced incandescence, photoionization mass spectrometry, and scanning mobility particle sizer) in ethylene-air-flames with the same total gas flow as investigated here. Their sampling system had a better spatial resolution by sampling from above and they have generated a dataset of these ethylene-air-flames. Size distributions of soot particles from flat ethylene flames were also measured by SMPS in the work of Zhao et al. (2003; 2005) and Maricq et al. (2004) to study soot formation processes in flames. In all of these experiments, the probe was designed to immediately dilute the flame-sampled soot particles with very high dilution ratios on the order of 10^4 to avoid particle-particle coagulation. In our setup, the sampled soot particles are diluted 10 mm upstream from the orifice of the sampling nozzle and dilution ratio is lower. Therefore, coagulation inside the sampling nozzle or during transfer at lower dilution ratio is probable as shown by Maricq (2007). As described in the experimental section, our transfer line consists of stainless steel and transfer time to the reactor is about 0.5 s. The soot particles are characterized at the reactor inlet and, thus, changes in the aerosol composition (coagulation and diffusion losses) during the transfer from the flame to the reactor are of minor importance to the investigated subject and will not be considered. However, particle-particle coagulation, can explain higher observed count median diameter of the sampled soot particles than in previous works (Maricq, 2004; Stirn et al., 2009; Zhao et al., 2003; Zhao et al., 2005) for similar flame and sampling conditions.

However, a detailed characterization of the particles by the SMPS at the reactor inlet is essential for the present analysis. All measured particles originate from the flame as

measurements with a HEPA filter have shown. The signal from the SMPS was nearly zero with the HEPA filter between the reactor inlet and the diluter. This indicates that no particles are released from the reactor at higher temperatures as observed for ceramic materials. Figure 3 shows measured PSDs before (inlet) and behind (outlet) the reactor without oxygen addition for the freshly-produced small, medium, and large flame soot particles as normalized particle number concentration dN/dlogDp vs. particle diameter taken with 64 channel resolution by the SMPS. All PSDs are log-normal or close to log-normal distributions, so that the count median diameter indicates the average particle size. No molecular oxygen could be measured by MBMS under pyrolytic conditions neither during sampling at 5 mm nor at 25 mm.

A reduction of the particle concentration and a change of the count median diameter are observed under pyrolytic conditions as seen in Figure 3. To verify if particle-particle coagulation may account for this behavior, the probability of coagulation inside the reactor will be estimated in the following. In general, particle-particle coagulation is a growth process due to collisions of particles and results in increasing count median diameter and decreasing number concentration (Hinds, 2011). Coagulation is strongly influenced by particle concentration and residence time. For a polydisperse aerosol, the coagulation process is enhanced when smaller particles with higher diffusion coefficients diffuse into bigger particles with their larger surface (Hinds, 2011). For the three investigated soot particle sizes, geometric standard deviation of the PSDs clearly shows that polydisperse aerosols are given and count median diameter of the particles is smaller than the mean free path of the gas molecules. Therefore, the coagulation model of a polydisperse aerosol in the free-molecule regime according to Lee and Chen (1984) can be applied to estimate the influence of coagulation inside the reactor under our conditions. The average coagulation coefficient K is

$$K = \frac{3\sqrt{3}}{\sqrt{2}}\left(\frac{\mu^2 CMD_0}{2\rho kT}\right)^{1/2} b\frac{2kT}{3\mu}\left[exp\left(\frac{25}{8}\ln^2\sigma\right) + exp\left(\frac{5}{8}\ln^2\sigma\right) + exp\left(\frac{1}{8}\ln^2\sigma\right)\right] \quad (1)$$

where μ is the dynamic gas viscosity, CMD_0 is the initial count median diameter, ρ is the particle density, k is the Boltzmann constant ($1.381 \cdot 10^{-23}$ J/K), T is the gas temperature, b is a constant defined by Lee and Chen (1984), and σ is the geometric standard deviation. A typical value of 1.5 g/cm^3 for nascent soot (Abid et al., 2008) was used for the particle density for soot particles sampled from the lower position (5 mm) in the flame. A higher value of 1.8 g/cm^3 for mature soot (Shaddix and Williams, 2009; Zhao et al., 2007) was used for the particles sampled from the higher position (25 mm) in the flame. The value of the constant b depends on the geometric standard deviation and is calculated by linear interpolation from the values provided by Lee and Chen (1984). The dynamic viscosity of a gas can be calculated for different temperatures according to

$$\mu = \mu_R\left(\frac{T}{T_R}\right)^{3/2}\left(\frac{T_R + S}{T + S}\right) \quad (2)$$

where μ_R is the reference gas viscosity, T_R is the reference temperature, and S is the Sutherland constant. Values of μ_R, T_R, and S for nitrogen are obtained from Chapman and Cowling (1970). Now, the final number concentration N at the outlet of the reactor after the residence time τ is

$$N = \frac{N_0}{1 + N_0 K\tau} \quad (3)$$

where N_0 is the initial number concentration at the reactor inlet. Finally, the final count median diameter CMD is:

$$CMD = CMD_0\left(\frac{N_0}{N}\right)^{1/3} \quad (4)$$

Table 3 lists the final number concentration and the count median diameter for the inlet PSDs from Figure 3 assuming polydisperse coagulation. An average temperature $T_{average}$ for the total length of the reactor was calculated from the temperature profiles and the adjusted oven

temperature T_{Oven}. The results show that coagulation of soot particles inside the reactor has only a minor effect at higher oven temperatures. For example, the small particles grow in size by 0.2 nm and number concentration decreases about 5%. In the work of Camacho et al. (2015) the time scale for coagulation is around 1 min for a comparable number concentration on the order of 10^7 cm^{-3}. A higher number concentration would have a significant effect as seen in the work of Maricq (2007) where number concentration is a factor of 100 higher than in our experiment.

The distribution of the small particles is unimodal showing one accumulation mode of primary particles and is shifted to slightly smaller CMD of 9.2 nm when passing the reactor at an oven temperature of 1123 K (Figure 3(a)). This shift is also observed at lower oven temperatures as seen in Figure 3(b) for a temperature of 773 K. Oxidation of soot particles by O_2 cannot be observed at this temperature and oxidation by H_2O or CO_2, which are sampled from the flame but are in comparison to O_2 only of minor importance in soot oxidation (Frenklach et al., 2018; Neoh et al., 1981), is also rather unlikely to contribute to the observed size reduction of soot particles in our experiment. Therefore, thermal effects seem to alter the mobility diameter of the particles.

A significant reduction of particle number concentration is seen for smaller particles passing the reactor. This particle loss is 58% at 773 K and 62% at 1123 K, respectively. Particle-particle coagulation would result in increasing particle diameter and only minor reduction in particle number concentration as shown in Table 3. Therefore, size reduction and particle loss may result by evaporation of volatile or semi-volatile material from the particle surface or deposition at the reactor walls during heating-up of the reactor. Nienow et al. (2005) also observed reduction of the peak mobility diameter for 30 nm soot particles after passing a quartz tube encased in a tube furnace in pure nitrogen gas. Their measured reduction was 0.552 nm at furnace temperature of 500 °C and 1.945 nm at 850 °C. Ma et al.

(2013) have reported about particle mass decreasing of larger size-selected soot particles of 100 and 200 nm in a 30 cm reactor (residence time of 5 s at room temperature) from room temperature to 600 °C and explained this observation that probably volatile organics evaporate from the particle surface. Maricq (2004) observed the decrease in particle concentration for both flame-sampled soot and diesel soot by using a thermodenuder, which heats the aerosol to 300 °C and removes volatile species from the gas phase before analyzing the aerosol by the differential mobility analyzer. A decrease of the particle diameter by 22-32% was also measured by Maricq (2007) after heating the size-selected soot particles, which were sampled from an ethylene-air-flame with an equivalence ratio of 2.0 at a height above the burner of 10 mm, to 330 °C in a heat pipe. Camacho et al. (2015) investigated the oxidation of nascent soot from laminar flames in a flow reactor with shorter residence times (0.20–0.22 s) and did not mentioned a particle loss or size reduction without the presence of oxygen. Differences in absolute number concentration between the PSDs of the small particles at different temperatures (773 and 1123 K) indicate a smaller loss of sampling efficiency of 20% over time. PSDs at 1123 K were measured before temperature-ramping of the soot oxidation process while PSDs at 773 K were measured at the end of the soot oxidation experiment.

Figure 3 shows that the PSD at the reactor inlet changes from unimodal to bimodal when vary the sampling position from 5 (Figure 3(a,b)) to 25 mm (Figure 3(c,d,e)) in the flame with Φ=1.85 to obtain the medium-sized soot particles. Maricq et al. (2003) measured bimodal particle size distributions in relatively rich premixed ethylene-air-flames at height above the burner of higher than 15 mm. A second mode in the particle size distribution of flame-sampled soot from a very rich ethylene-air-flame (equivalence ratio of 2.5) also appeared at a height above the burner of 7 mm in measurements of Öktem et al. (2005). The transition from unimodal to bimodal distribution was observed at lower equivalence ratios by

Stirn et al. (2009) for an ethylene-air-flame with Φ=1.9 at a height above the burner of 14 mm. They interpreted it as a soot precursor mode and a soot mode. Here, both modes are in the particle diameter range of typical accumulation modes (10–100 nm) observed in flames (Maricq, 2009). PSDs of the medium-sized particles change from bimodal to unimodal with a broader shoulder after passing the reactor at pyrolytic conditions at 673 and 1173 K. At room temperature the PSD stays bimodal at the reactor outlet (Figure 3(e)), but the two observed modes are shifted together. As a result, the count median diameter alters. Number concentration is slightly lower, so that particle loss is only 13–16% for the medium-sized particles. The PSD from the flame with Φ=2.00 gives the largest particles as seen from Figure 3(f) and has a second mode at about 150 nm. The two modes of the distribution are also present at the reactor outlet at 873 K, while for the medium-sized particles the two maxima of the inlet distribution disappeared at the reactor outlet as discussed before. Again, the first maxima shifted to higher mean diameter and the second maxima to smaller one. One possible explanation for this behavior could be a restructuring that takes place. Particle number concentration remains the same for the large particles. The small mode at about 2 and 4 nm for the small (Figure 3(a)) and medium-sized soot particles (Figure 3(c)) is observed after pyrolysis at higher temperatures at the reactor outlet and might be a measurement artifact due to an insufficient retrace time period (i.e., time of the electrode to reach initial voltage). Sizes are in the typical particle diameter range of nucleation modes (Maricq, 2009).

Particle size distributions during the oxidation process and oxidation rates

PSDs at the reactor outlet during oxidation process with 6150 ppm O_2 for the small and medium-sized particles and with 7500 ppm O_2 for the large particles are shown in Figure 4 as function of the oven temperature in 3D and 2D contour plots, respectively. At lowest temperatures, when oxidation reactions of soot particles not yet take place, distributions of

the small and medium-sized particles are unimodal, while large particles have two modes as already discussed before. Addition of O_2 to the aerosol behind the ejector nozzle of the Dekati diluter does not change the initial PSD at the reactor inlet and oxidation of soot starts for the small soot particles at lower oven temperatures of approx. 940 K. At about 990 K, oxidation of medium-sized particles starts and slightly higher temperatures (~1000 K) are needed for initial oxidation of the large particles. Both medium-sized and large soot particles are sampled from the post-flame region of the ethylene-air-flame. Therefore, it is rather mature soot and reactivity is similar. The small soot particles from the lower sampling position of the flame (soot inception region) are probably nascent or young soot. For comparison, Camacho et al. (2015) have sampled nascent soot from a premixed ethylene-flame (Φ=2.07) by a stagnation-surface probe at 8 mm above the burner surface.

Small and medium-sized soot particles are totally oxidized above 1050 and 1080 K, respectively (see Figure 4(a,b)). The large particles are totally oxidized at oven temperatures above 1175 K. The PSDs shift to smaller count median diameter with soot oxidation. This can be clearly seen for the medium and large distributions in Figure 4(b,c). The soot source and the sampling system are stable enough for the continuous temperature ramping from 1173–773 K for the flame with an equivalence ratio of 1.85 (small and medium-sized particles). For the richer flame with an equivalence ratio of 2.00, the clogging of the sampling nozzle of the diluter is under these conditions an issue. During the oxidation experiment the signal often decreases so that soot deposit at the nozzle had to be removed. Therefore, some dips can be seen in the contour plot of the large distribution from blowing off the soot deposit.

Soot oxidation rates ω for the oxidation of soot by molecular oxygen can be calculated based on a simple shrinking sphere model (Camacho et al., 2015; Vander Wal and Tomasek, 2003) according to equation (5):

$$\frac{dm}{dt} = \omega \cdot A \tag{5}$$

Soot oxidation takes place at the particle surface A and is expressed as mass loss dm over time dt. If the density of the soot ρ is constant, the soot oxidation rate ω in g/cm^2·s can also be expressed by equation (6) considering the change of the particle diameter dDp over time:

$$\omega = \frac{\rho}{2} \cdot \frac{dDp}{dt} \tag{6}$$

For our experiment, dt is the residence time of the particles in the heated length of the reactor where the oxidation takes place and dDp is the difference of the initial count median diameter of the PSD without oxidation and the count median diameter of the PSD at the outlet of the reactor after oxidation. For the initial count median diameter, a PSD at the outlet of the reactor at the lowest oven temperature of the ramping measurement is appropriate to consider only changes in size reduction by the oxidation process itself. As discussed before, size reduction was also observed at pyrolytic conditions without oxidation taking place. Soot oxidation rates can be calculated at oven temperatures where size reduction of the count median diameter is observed. Soot density was estimated to be 1.8 g/cm^3 for the medium-sized and large soot particles. This is a typical value for mature soot (Shaddix and Williams, 2009; Zhao et al., 2007) and lies between nascent soot (Camacho et al., 2015) and amorphous carbon (Vander Wal and Tomasek, 2003). The same value for the medium-sized and large particles was used, because both were sampled from the post-flame region and the particle core density can be related to mature soot. Of course, larger particles may not be spherical because aggregates of smaller primary particles are present and measured modes are in the accumulation range. Therefore, the effective density of the agglomerate can be much lower than the material density of the primary particle core and decreases with increasing particle diameter as shown by Ghazi et al. (2013) and Maricq and Xu (2004) for soot sampled from ethylene-air-flames. However, the used model of the shrinking spheres is based on the

assumption of spherical particles. Therefore, the density of the primary particle core is used and 1.8 g/cm^3 is an appropriate value for the density of mature soot. Figure 5 shows the calculated oxidation rates for the medium-sized and large soot particles in comparison to predictions of the oxidation rates obtained from the NSC model (Walls and Strickland-Constable, 1964) for a partial pressure of oxygen of $6.15 \cdot 10^{-3}$ atm (6150 ppm) and $7.5 \cdot 10^{-3}$ atm (7500 ppm). The oven temperatures were converted in actual gas-phase temperatures by the scaling law (see Figure 2(a)), which was determined in the isothermal zone of the reactor. The results show that calculated values of the soot oxidation rates for the flame-sampled soot are about a factor of 3–4 higher than predicted values by the NSC model indicating that our investigated soot is more reactive than pyrolytic graphite. The NSC model was originally developed from high-temperature measurements (1000–2400 °C), but is also reasonable for lower temperatures smaller than 1000 °C (Nienow et al., 2005). Camacho et al. (2015) have observed higher reactivity of freshly-produced flame soot, too. Their oxidation rates for the oxidation of nascent soot were even a factor of 10 higher than values by the NSC model. Similar results were made by Ghiasi et al. (2016), who have measured oxidation rates of flame soot from different fuels and flame conditions which were up to one order of magnitude higher than the NSC model. Therefore, observed reactivity of the medium-sized and large particles is between the reactivity of pyrolytic graphite and nascent soot. Flame-sampled soot from the post-flame region at 25 mm of the ethylene-air-flames is rather mature soot than nascent soot so that this observation is plausible. Differences in the reactivity of different types of soot are not unusual, e.g., Vander Wal and Tomasek (2003) measured differences in oxidation rates by more than 400% for soot particles generated by pyrolysis from different fuels. However, in other studies soot oxidation rates smaller than the NSC model were also observed for flame soot (Higgins et al., 2002) and diesel soot (Higgins et al., 2003).

Oxidation rates from the experiment with the small particles are not shown and give unreasonable results with values significantly smaller (more than a factor of 5) than predicted values by the NSC model. This might be because of the very slight size reduction of the particles measured by SMPS during soot oxidation. The small particles were sampled from a lower flame position. Soot from this position should be less aged and reactivity should rather be higher than for the medium-sized and large particles because the different sampling positions of 5 and 25 mm result in different reaction times for soot formation in the flame. Soot sampled from 5 mm is rather nascent soot (Apicella et al., 2018) and an appropriate value for nascent soot is 1.5 g/cm^3 (Abid et al., 2008). Other effects which may influence the soot oxidation in our experiments, e.g., oxidation by other oxidants formed during the oxidation of sampled flame species like the OH radical or competitive particle growth, are not considered herein. Recently, Frenklach et al. (2018) have modeled the low-temperature oxidation results of nascent soot by Camacho et al. (2015). They even had to consider catalytic decomposition of water vapor on the reactor walls to provide additional H and OH radicals to match the experimental values of Camacho et al. (2015) with their model. Additionally, it was assumed in our calculation of soot oxidation rates that all particles are spherical to apply the shrinking sphere model, but soot particles could have elongated shapes due to agglomeration (Camacho et al., 2015). However, the experimental soot oxidation rates presented here will give a rough value for the reactivity of the investigated soot, but investigations under further conditions are necessary.

Molecular gas-phase species during the oxidation process

Molecular gas-phase species were measured simultaneously during the soot oxidation at the reactor outlet by MBMS. The quantification process to obtain the mole fraction profiles follows the procedure described by Oßwald and Köhler (2015) using nitrogen as the

reference species. Mole fraction profiles of some molecular gas-phase species are shown for the measurements of the flame with an equivalence ratio of 1.85 in Figure 6. All detectable hydrocarbons have a mole fraction profile showing typical fuel behavior (e.g., C_2H_2 or C_6H_6 as seen in Figure 6(a,c)) and are therefore directly sampled from the flame, while a few oxygenated species like formaldehyde (CH_2O) or ketene (CH_2CO) are intermediates formed during the oxidation process inside the reactor. The lower sampling position in the flame (small PSD) is in the reaction zone of the flame where combustion intermediates are formed and mole fraction of sampled acetylene is significantly higher than for the higher sampling position (medium PSD). As a result, intermediates which are formed during the oxidation process in the reactor, like formaldehyde, are also observed in higher concentrations. One of the species with the highest observed mass in detectable amounts was naphthalene ($C_{10}H_8$). Largest observed oxygenated species was on *m/z* 94 and can be related to phenol (C_6H_5OH). Comparison of the mole fraction profiles with the total number concentration of soot particles shows that the soot oxidation is clearly separated from the oxidation of the flame species as shown here for vinylacetylene (C_4H_4) and benzene (C_6H_6) in Figure 6(c). For both sampling positions, the oxidation of flame species starts at lower temperatures before soot oxidation takes place. It was also observed that some sampled flame species have different oxidation behavior, e.g., oxidation of C_4H_4 starts a little earlier at lower temperatures than oxidation of C_6H_6.

The major species (i.e., H_2, H_2O, O_2, and CO_2) have similar mole fraction profiles for the experiments with the small and medium-sized soot particles (see Figure 6(b)). Detection of CO is not possible by the MBMS at the reactor outlet despite the high mass resolution of the reflectron TOF mass spectrometer because of the high concentration of the dilution gas nitrogen. Nitrogen has to be used because of the SMPS spectrometer. The mole fraction of the CO_2 further increases due to oxidation of soot particles also after flame-sampled

hydrocarbons are already consumed and mole fraction of O_2 continues to decrease accordingly. Differences between the two sampling positions can be clearly seen from Figure 6(b) for the mole fraction of water which stays nearly constant for the measurement with the medium-sized soot particles but further increases slightly at higher reactor temperatures (> 975 K) for the measurement with the small particles. This observation might reflect the fact, that the medium particles are rather mature soot with distinctly higher C/H ratio than the small particles which are rather nascent soot. The atomic C/H ratio generally increases when soot ages and is typically about 8:1 for mature soot (Calcote, 1981; Zhao et al., 2007). In contrast, nascent soot has the highest hydrogen content and the C/H ratio is close to unity (Omidvarborna et al., 2015; Zhao et al., 2007).

Reproducibility of the soot oxidation experiment

We have measured oxidation of small and medium-sized particles three times to check reproducibility of the experiment and find good agreement between these measurements for both measurement techniques, i.e., the mole fraction profiles measured by MBMS and the particle size distributions measured by the SMPS spectrometer, as seen in Figure 6(d) for measured total number concentration of soot particles and mole fractions of acetylene and formaldehyde from two series of soot oxidation of small particles. The measurement of stable flame gases (H_2, H_2O, C_2H_2, and CO_2) and the diluent gas (N_2) by the QMS at the inlet of the reactor allows monitoring the initial gas-phase composition and ensures the long-term stability during the soot oxidation experiments. If the sampling nozzle starts clogging, signal intensity of sampled flame gases (e.g., C_2H_2 or CO_2) will drop. N_2 and O_2 are added behind the sampling nozzle and their signal will not be affected by clogging of the nozzle. For both equivalence ratios, the signal intensity of the flame gases decreases during the oxidation experiments over time. While this is minor for Φ=1.85, the clogging of the sampling nozzle is

a significant challenge for the higher equivalence ratio at Φ=2.00, where it is necessary to blow out the accumulated solid soot particles inside the nozzle several times during the measurements. Otherwise, the sampling nozzle would be completely clogged. Nevertheless, important insights about soot oxidation processes can also be obtained from the measurement of the large particles as shown before. The complete dataset for the oxidation of the small and medium-sized particles, i.e., particle size distributions and mole fraction profiles of molecular gas-phase species, are provided in the supplemental material. Besides the normalized number concentration, normalized surface area concentration was also calculated under assumption of spherical particles.

Conclusions

The oxidation of soot particles by molecular oxygen was studied under well-controlled conditions between 773–1273 K at atmospheric pressure in a flow reactor. Soot particles of three different sizes were produced by variation of flame conditions and sampling position in a laminar, premixed ethylene-air-flame. This soot source is stable for moderate equivalence ratios and continuous temperature ramping. Total oxidation can be achieved under the investigated conditions. The flame with an equivalence ratio of 1.85 gives a reproducible data set for the oxidation of small and medium-sized soot particles and the sampled flame species, i.e., for measured PSDs by scanning mobility particle sizer and mole fraction profiles of molecular gas-phase species by molecular-beam mass spectrometry. Small soot oxidation products (e.g., formaldehyde, ketene) and sampled molecules from the flame (e.g., acetylene, benzene) were quantified by molecular-beam mass spectrometry. Oxidation of soot particles of different sizes starts at different temperatures, but for all investigated particles at higher temperatures than oxidation of gas-phase species. Calculated soot oxidation rates show that medium-sized and large soot particles from the post-flame region are higher in the

investigated temperature range than the values predicted by the Nagle-Strickland-Constable model. Soot particles from this flame region are therefore more reactive than pyrolytic graphite. The presented dataset for the oxidation of soot particles of different sizes in a wide temperature range may help to validate existing soot models.

Funding

This work was supported by the European Union within the project SOPRANO Horizon 2020 under Grant Agreement No. 690724.

References

Abid, A.D., Heinz, N., Tolmachoff, E.D., Phares, D.J., Campbell, C.S., and Wang, H. 2008. On evolution of particle size distribution functions of incipient soot in premixed ethylene–oxygen–argon flames. *Combust. Flame,* **154**, 775-788.

Apicella, B., Ciajolo, A., Tregrossi, A., Abrahamson, J., Vander Wal, R.L., and Russo, C. 2018. HRTEM and EELS investigations of flame-formed soot nanostructure. *Fuel,* **225**, 218-224.

Bockhorn, H. (Ed.) 1994. *Soot Formation in Combustion: Mechanisms and Models,* Springer, Berlin.

Cadman, P., and Denning, R.J. 1996. Oxidation rates of soot particulates by oxygen in the temperature range 1500–3500 K determined using a shock tube. *J. Chem. Soc., Faraday Trans.,* **92**, 4159-4165.

Calcote, H.F. 1981. Mechanisms of soot nucleation in flames - A critical review. *Combust. Flame,* **42**, 215-242.

Camacho, J., Tao, Y., and Wang, H. 2015. Kinetics of nascent soot oxidation by molecular oxygen in a flow reactor. *Proc. Combust. Inst.,* **35**, 1887-1894.

Chan, M.-L., Moody, K.N., Mullins, J.R., and Williams, A. 1987. Low-temperature oxidation of soot. *Fuel,* **66**, 1694-1698.

Chapman, S., and Cowling, T.G. 1970. *The Mathematical Theory of Non-Uniform Gases,* 3rd ed., Cambridge Univerity Press, Cambridge.

Echavarria, C.A., Jaramillo, I.C., Sarofim, A.F., and Lighty, J.S. 2011. Studies of soot oxidation and fragmentation in a two-stage burner under fuel-lean and fuel-rich conditions. *Proc. Combust. Inst.,* **33**, 659-666.

Echavarria, C.A., Jaramillo, I.C., Sarofim, A.F., and Lighty, J.S. 2012. Burnout of soot particles in a two-stage burner with a JP-8 surrogate fuel. *Combust. Flame,* **159**, 2441-2448.

Fenimore, C.P., and Jones, G.W. 1967. Oxidation of soot by hydroxyl radicals. *J. Phys. Chem.,* **71**, 593-597.

Frenklach, M., Liu, Z., Singh, R.I., Galimova, G.R., Azyazov, V.N., and Mebel, A.M. 2018. Detailed, sterically-resolved modeling of soot oxidation: Role of O atoms, interplay with particle nanostructure, and emergence of inner particle burning. *Combust. Flame,* **188**, 284-306.

Garo, A., Prado, G., and Lahaye, J. 1990. Chemical aspects of soot particles oxidation in a laminar methane-air diffusion flame. *Combust. Flame,* **79**, 226-233.

Ghazi, R., Tjong, H., Soewono, A., Rogak, S.N., and Olfert, J.S. 2013. Mass, mobility, volatility, and morphology of soot particles generated by a McKenna and inverted burner. *Aerosol Sci. Technol.,* **47**, 395-405.

Ghiassi, H., Jaramillo, I.C., and Lighty, J.S. 2016. Kinetics of soot oxidation by molecular oxygen in a premixed flame. *Energy Fuels,* **30**, 3463-3472.

Gilot, P., Bonnefoy, F., Marcuccilli, F., and Prado, G. 1993. Determination of kinetic data for soot oxidation. Modeling of competition between oxygen diffusion and reaction during thermogravimetric analysis. *Combust. Flame,* **95**, 87-100.

Guo, H., Anderson, P.M., and Sunderland, P.B. 2016. Optimized rate expressions for soot oxidation by OH and O_2. *Fuel,* **172**, 248-252.

Higgins, K.J., Jung, H., Kittelson, D.B., Roberts, J.T., and Zachariah, M.R. 2002. Size-selected nanoparticle chemistry: Kinetics of soot oxidation. *J. Phys. Chem. A,* **106**, 96-103.

Higgins, K.J., Jung, H., Kittelson, D.B., Roberts, J.T., and Zachariah, M.R. 2003. Kinetics of diesel nanoparticle oxidation. *Environ. Sci. Technol.,* **37**, 1949-1954.

Hinds, W.C. 2011. Physical and Chemical Processes in Aerosol Systems. In Kulkarni, P., Baron, P.A., and Willeke, K. (Eds.), *Aerosol Measurement*, 3rd ed., Wiley, Hoboken, pp. 31-40.

Jaramillo, I.C., Gaddam, C.K., Vander Wal, R.L., Huang, C.-H., Levinthal, J.D., and Lighty, J.S. 2014. Soot oxidation kinetics under pressurized conditions. *Combust. Flame,* **161**, 2951-2965.

Jaramillo, I.C., Gaddam, C.K., Vander Wal, R.L., and Lighty, J.S. 2015. Effect of nanostructure, oxidative pressure and extent of oxidation on model carbon reactivity. *Combust. Flame,* **162**, 1848-1856.

Jung, H., Kittelson, D.B., and Zachariah, M.R. 2004. Kinetics and visualization of soot oxidation using transmission electron microscopy. *Combust. Flame,* **136**, 445-456.

Kathrotia, T., Oßwald, P., Köhler, M., Slavinskaya, N., and Riedel, U. 2018. Experimental and mechanistic investigation of benzene formation during atmospheric pressure flow reactor oxidation of n-hexane, n-nonane, and n-dodecane below 1200 K. *Combustion and Flame,* **194**, 426-438.

Khosousi, A., and Dworkin, S.B. 2015. Detailed modelling of soot oxidation by O_2 and OH in laminar diffusion flames. *Proc. Combust. Inst.,* **35**, 1903-1910.

Kim, C.H., Xu, F., and Faeth, G.M. 2008. Soot surface growth and oxidation at pressures up to 8.0 atm in laminar nonpremixed and partially premixed flames. *Combust. Flame,* **152**, 301-316.

Köhler, M., Oßwald, P., Krüger, D., and Whitside, R. 2018. Combustion chemistry of fuels: Quantitative speciation data obtained from an atmospheric high-temperature flow reactor with coupled molecular-beam mass spectrometer. *J. Vis. Exp.*, **132**, e56965.

Lee, K.W., and Chen, H. 1984. Coagulation rate of polydisperse particles. *Aerosol Sci. Technol.,* **3**, 327-334.

Liu, C., Zhu, L., Gao, Z., Li, H., and Huang, Z. 2018. Effects of molecular O_2 and NO_2 on particle size distribution, morphology and nanostructure of diffusion flame soot oxidized in a flow reactor. *Fuel,* **234**, 335-346.

Liu, Y., Sun, X., Sethi, V., Nalianda, D., Li, Y.-G., and Wang, L. 2017. Review of modern low emissions combustion technologies for aero gas turbine engines. *Prog. Aerosp. Sci.,* **94**, 12-45.

Ma, X., Zangmeister, C.D., and Zachariah, M.R. 2013. Soot oxidation kinetics: A comparison study of two tandem ion-mobility methods. *J. Phys. Chem. C,* **117**, 10723-10729.

Maricq, M.M. 2004. Size and charge of soot particles in rich premixed ethylene flames. *Combust. Flame,* **137**, 340-350.

Maricq, M.M. 2007. Coagulation dynamics of fractal-like soot aggregates. *J. Aerosol Sci.,* **38**, 141-156.

Maricq, M.M. 2009. An examination of soot composition in premixed hydrocarbon flames via laser ablation particle mass spectrometry. *J. Aerosol Sci.,* **40**, 844-857.

Maricq, M.M., Harris, S.J., and Szente, J.J. 2003. Soot size distributions in rich premixed ethylene flames. *Combust. Flame,* **132**, 328-342.

Maricq, M.M., and Xu, N. 2004. The effective density and fractal dimension of soot particles from premixed flames and motor vehicle exhaust. *J. Aerosol Sci.,* **35**, 1251-1274.

Nagle, J., and Strickland-Constable, R.F. 1962. Oxidation of carbon between 1000–2000°C. *Proceedings of the Fifth Conference on Carbon*, Pergamon, pp. 154-164.

Neoh, K.G., Howard, J.B., and Sarofim, A.F. 1981. Soot Oxidation in Flames. In Siegla, D.C., and Smith, G.W. (Eds.), *Particulate Carbon*, Springer, Boston, pp. 261-282.

Neoh, K.G., Howard, J.B., and Sarofim, A.F. 1985. Effect of oxidation on the physical structure of soot. *Proc. Combust. Inst.,* **20**, 951-957.

Nienow, A.M., Roberts, J.T., and Zachariah, M.R. 2005. Surface chemistry of nanometer-sized aerosol particles: Reactions of molecular oxygen with 30 nm soot particles as a function of oxygen partial pressure. *J. Phys. Chem. B,* **109**, 5561-5568.

Öktem, B., Tolocka, M.P., Zhao, B., Wang, H., and Johnston, M.V. 2005. Chemical species associated with the early stage of soot growth in a laminar premixed ethylene-oxygen-argon flame. *Combust. Flame,* **142**, 364-373.

Omidvarborna, H., Kumar, A., and Kim, D.-S. 2015. Recent studies on soot modeling for diesel combustion. *Renew. Sustain. Energy Rev.,* **48**, 635-647.

Oßwald, P., and Köhler, M. 2015. An atmospheric pressure high-temperature laminar flow reactor for investigation of combustion and related gas phase reaction systems. *Rev. Sci. Instrum.,* **86**, 105109.

Oßwald, P., Whitside, R., Schäffer, J., and Köhler, M. 2017. An experimental flow reactor study of the combustion kinetics of terpenoid jet fuel compounds: Farnesane, p-menthane and p-cymene. *Fuel,* **187**, 43-50.

Park, C., and Appleton, J.P. 1973. Shock-tube measurements of soot oxidation rates. *Combust. Flame,* **20**, 369-379.

Puri, R., Santoro, R.J., and Smyth, K.C. 1994. The oxidation of soot and carbon monoxide in hydrocarbon diffusion flames. *Combust. Flame,* **97**, 125-144.

Roth, P., Brandt, O., and Von Gersum, S. 1991. High temperature oxidation of suspended soot particles verified by CO and CO_2 measurements. *Proc. Combust. Inst.,* **23**, 1485-1491.

Shaddix, C.R., and Williams, T.C. 2009. Soot structure and dimensionless extinction coefficient in diffusion flames: Implications for index of refraction. In Bockhorn, H., D`Anna, A., Sarofim, A.F., and Wang, H. (Eds.), *Combustion Generated Fine Carbonaceous Particles*, KIT Scientific Publishing, Karlsruhe, pp. 17-33.

Stanmore, B.R., Brilhac, J.F., and Gilot, P. 2001. The oxidation of soot: A review of experiments, mechanisms and models. *Carbon,* **39**, 2247-2268.

Stirn, R., Baquet, T.G., Kanjarkar, S., Meier, W., Geigle, K.P., Grotheer, H.H., Wahl, C., and Aigner, M. 2009. Comparison of particle size measurements with laser-induced incandescence, mass spectroscopy, and scanning mobility particle sizing in a laminar premixed ethylene/air flame. *Combust. Sci. Technol.,* **181**, 329-349.

Vander Wal, R.L., and Tomasek, A.J. 2003. Soot oxidation: Dependence upon initial nanostructure. *Combust. Flame,* **134**, 1-9.

Walls, J.R., and Strickland-Constable, R.F. 1964. Oxidation of carbon between 1000-2400°C. *Carbon,* **1**, 333-338.

Zhao, B., Uchikawa, K., and Wang, H. 2007. A comparative study of nanoparticles in premixed flames by scanning mobility particle sizer, small angle neutron scattering, and transmission electron microscopy. *Proc. Combust. Inst.,* **31**, 851-860.

Zhao, B., Yang, Z., Li, Z., Johnston, M.V., and Wang, H. 2005. Particle size distribution function of incipient soot in laminar premixed ethylene flames: effect of flame temperature. *Proc. Combust. Inst.,* **30**, 1441-1448.

Zhao, B., Yang, Z., Wang, J., Johnston, M.V., and Wang, H. 2003. Analysis of soot nanoparticles in a laminar premixed ethylene flame by scanning mobility particle sizer. *Aerosol Sci. Technol.,* **37**, 611-620.

Table 1. Flame conditions of ethylene-air-flames to generate fresh soot particles.

Φ	C_2H_4 [slm]	Air [slm]	Co-flow [slm]	*v* [cm/s]
1.85	1.14 (1.428 g/min)	8.86	4	6.4
2.00	1.23 (1.540 g/min)	8.77	14	6.4

Table 2. Investigated soot particles from ethylene-air-flames.

Φ	Sampling [mm]	PSD	CMD [nm]	σ
1.85	5	Small	12.0	1.5
1.85	25	Medium	28.5	1.7
2.00	25	Large	63.1	1.7

Table 3. Calculated number concentration and count median diameter due to coagulation for the particle size distributions at the reactor inlet.

	Inlet particle size distribution					
	a	b	c	d	e	f
T_{Oven} [K]	1123	773	1173	673	298	873
$T_{average}$ [K]	928	671	965	597	298	744
τ [s]	1.75	2.42	1.69	2.72	5.46	2.19
CMD_0 [nm]	12.0	10.9	28.5	28.5	34.8	63.1
σ	1.489	1.475	1.682	1.682	1.646	1.743
N_0 [10^7 cm^{-3}]	1.472	1.077	1.190	1.190	1.489	1.053
μ [10^{-5} Pa·s]	3.7942	3.1058	3.8842	2.8813	1.7706	3.3142
ρ [g/cm^3]	1.5	1.5	1.8	1.8	1.8	1.8
b	0.7650	0.7633	0.7917	0.7917	0.7867	0.8002
K [10^{-15} m^3/s]	2.066	1.6538	3.609	2.839	2.129	5.0646
N [10^7 cm^{-3}]	1.398	1.032	1.109	1.090	1.269	0.9429
CMD	12.2	11.1	29.2	29.4	36.7	65.5
N/N_0	0.949	0.959	0.932	0.916	0.852	0.895

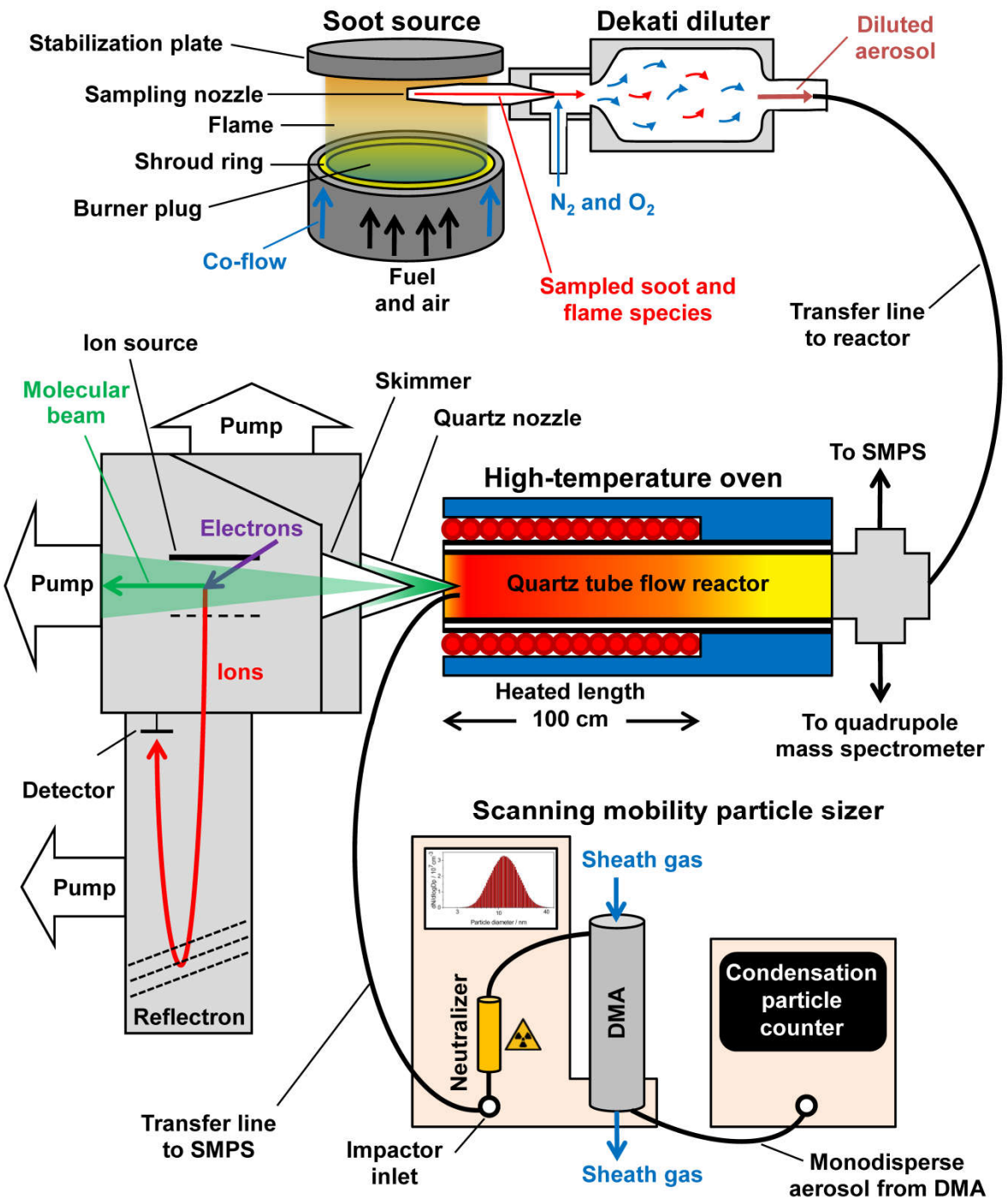

Figure 1. Schematic diagram of the experimental setup used for the investigation of soot oxidation in a flow reactor.

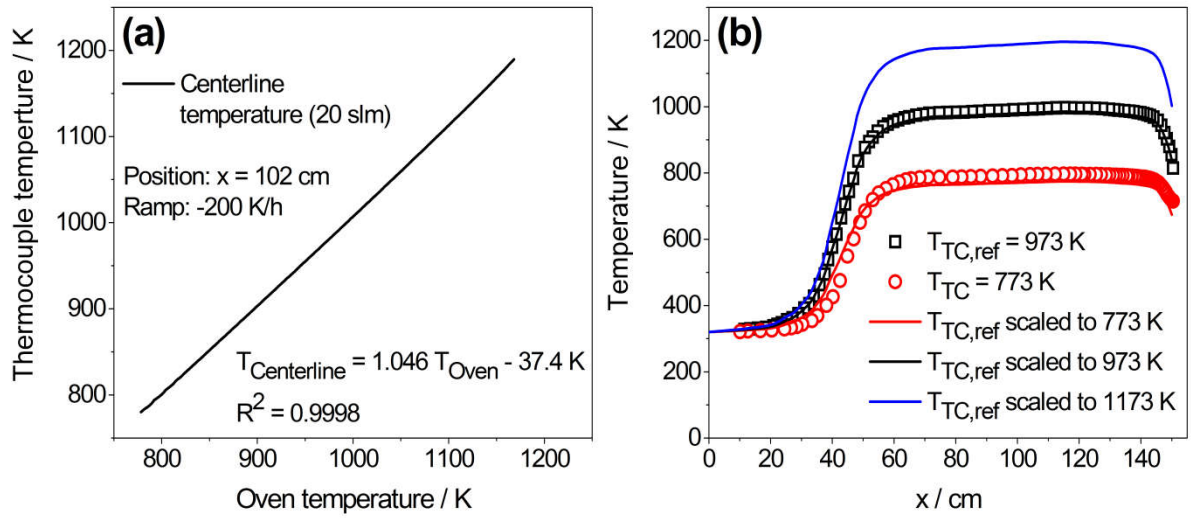

Figure 2. (a) Centerline temperature for continuous variation of the oven temperature for non-reactive nitrogen flow of 20 slm and (b) measured centerline temperature profiles for two oven temperatures (symbols) and scaled temperature profiles of 773, 973, and 1173 K (lines).

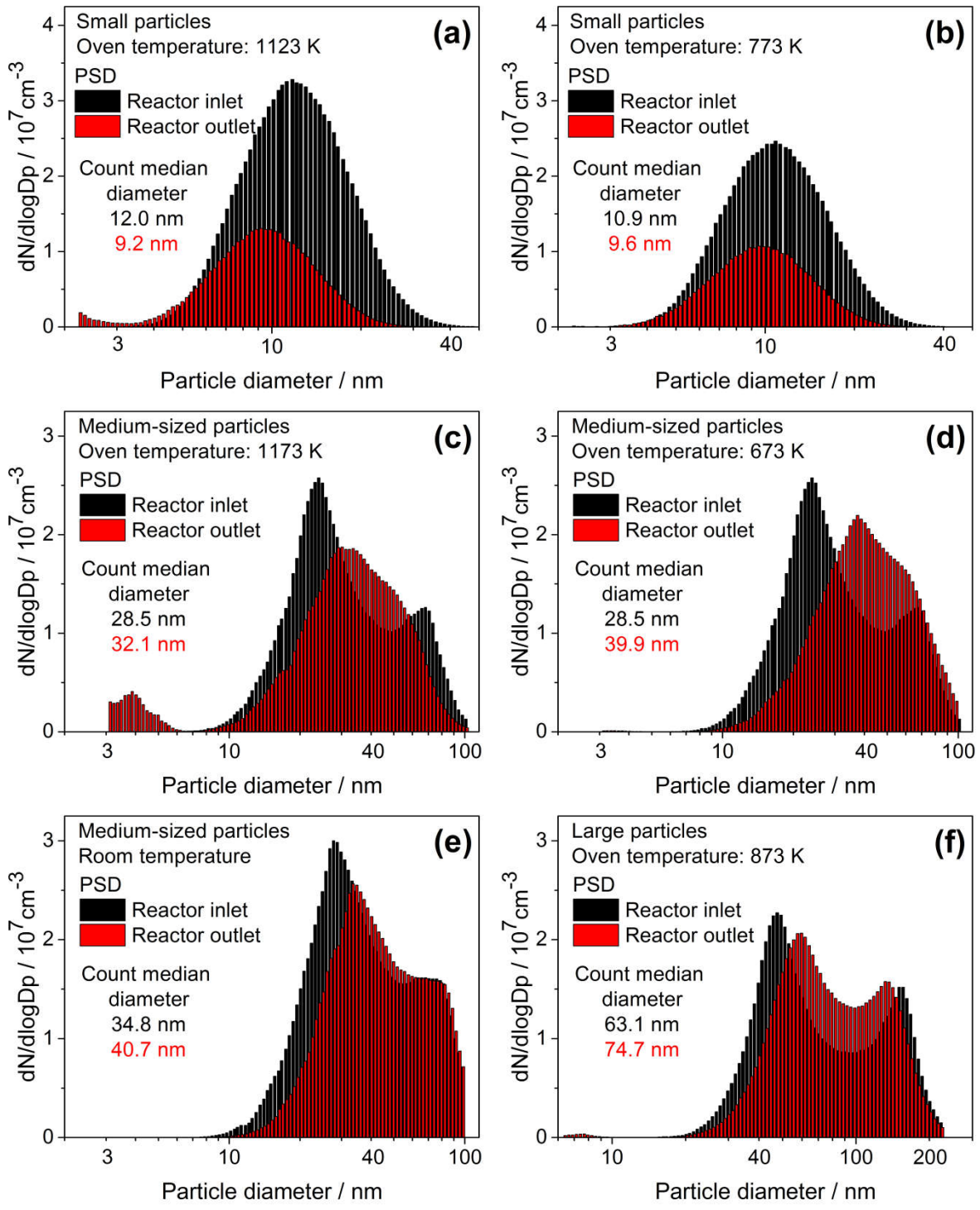

Figure 3. Particle size distributions at the reactor inlet (black) and outlet (red) for the (a,b,c) small, (d,e) medium-sized, and (f) large soot particles measured at different oven temperatures.

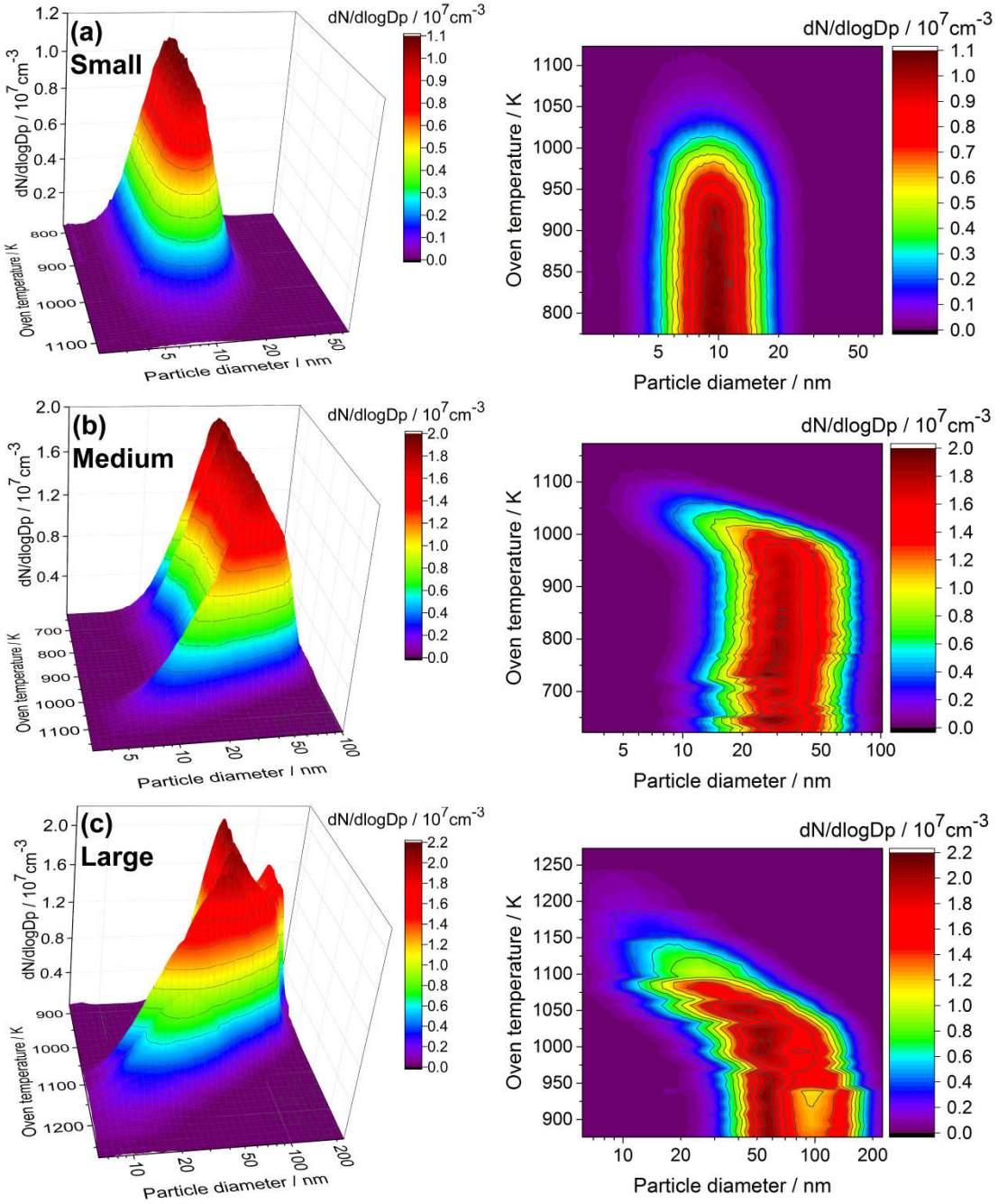

Figure 4. 3D and 2D contour plots of the particle size distributions as function of the oven temperature for the soot oxidation experiments of (a) small (top row), (b) medium-sized (middle row), and (c) large particles (bottom row).

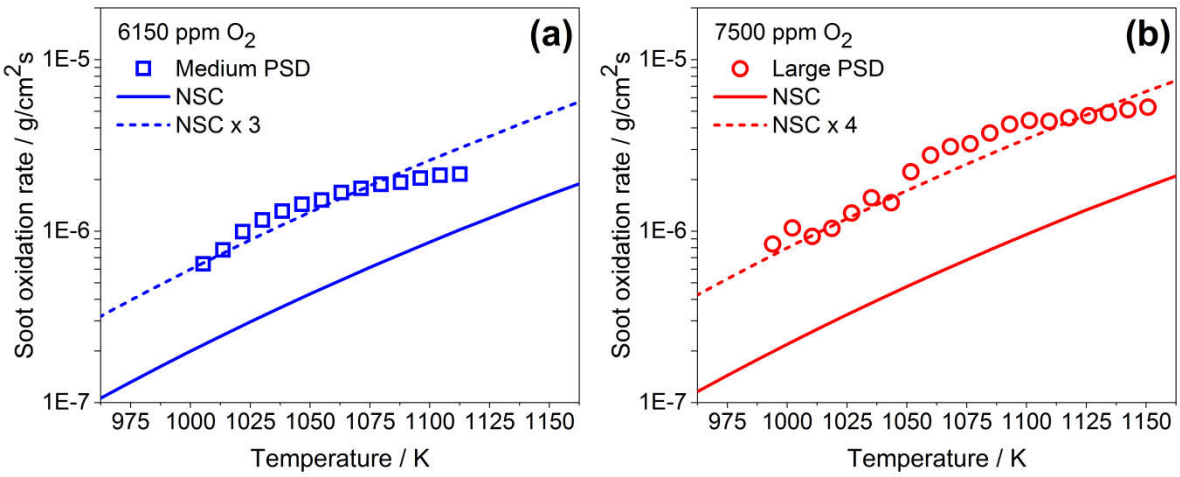

Figure 5. Soot oxidation rates of the (a) medium-sized and (b) large soot particles for different oven temperatures assuming a particle density of 1.8 g/cm^3 and spherical shape in comparison to the values predicted by the NSC model.

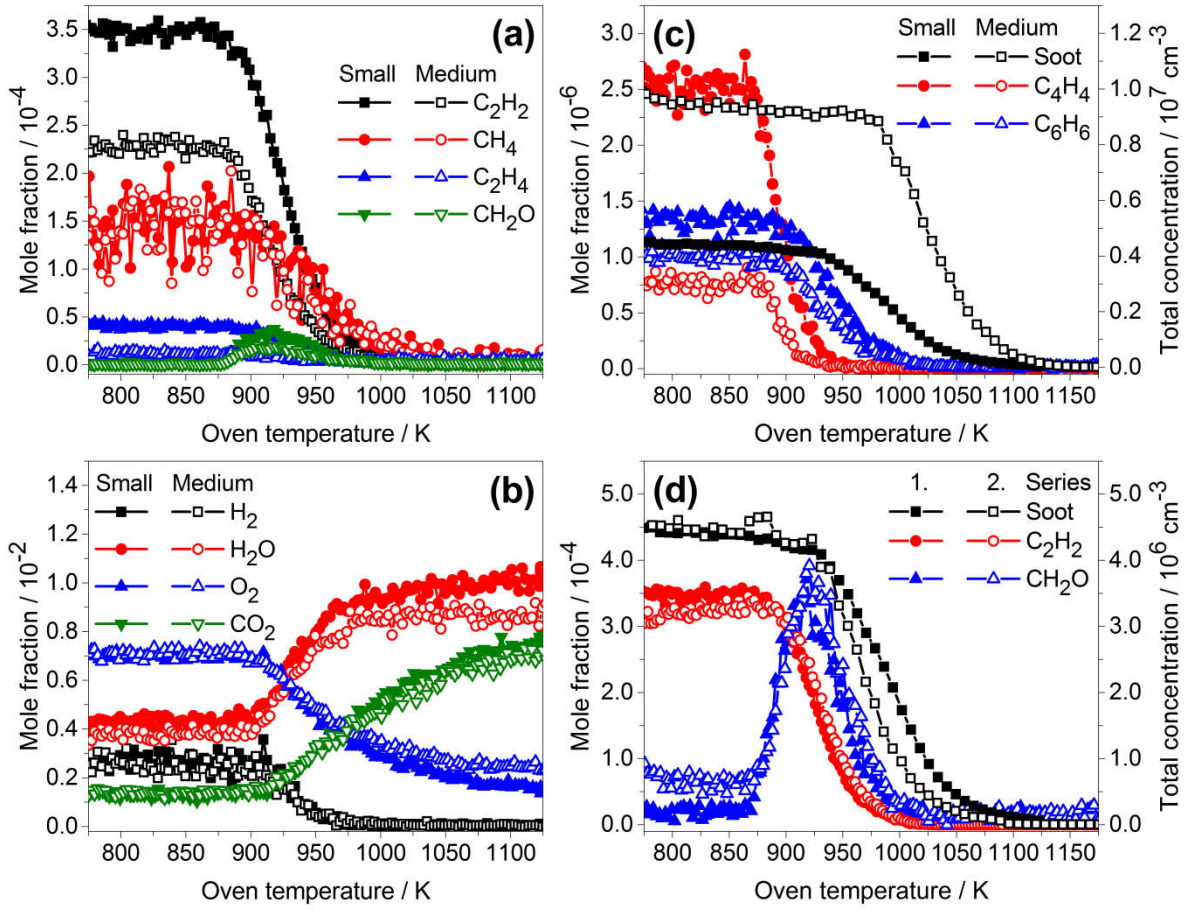

Figure 6. (a,b) Mole fraction profiles of some molecular gas-phase species observed during oxidation of small and medium-sized particles. (c) Comparison of mole fraction profiles with total number concentration of small and medium-sized soot particles. (d) Reproducibility of two series of measurements for the small particles.